PHOTONICS Research

Dual-band and ultra-broadband photonic spin-orbit interaction for electromagnetic shaping based on single-layer silicon metasurfaces

Xin Xie,[1,2] Mingbo Pu,[1,2] Xiong Li,[1,2] Kaipeng Liu,[1,2,3] Jinjin Jin,[1,2] Xiaoliang Ma,[1,2] and Xiangang Luo[1,2,*]

[1]State Key Laboratory of Optical Technologies on Nano-Fabrication and Micro-Engineering, Institute of Optics and Electronics, Chinese Academy of Sciences, Chengdu 610209, China
[2]School of Optoelectronics, University of Chinese Academy of Sciences, Beijing 100049, China
[3]School of Optoelectronic Science and Engineering, University of Electronic Science and Technology of China, Chengdu 611731, China
*Corresponding author: lxg@ioe.ac.cn

Achieving electromagnetic wave scattering manipulation in the multispectral and broad operation band has been a long pursuit in stealth applications. Here, we present an approach by using single-layer metasurfaces composed of space-variant amorphous silicon ridges tiled on a metallic mirror, to generate high-efficiency dual-band and ultra-wideband photonic spin-orbit interaction and geometric phase. Two scattering engineered metasurfaces have been designed to reduce specular reflection; the first one can suppress both specular reflectances at 1.05–1.08 μm and 5–12 μm below 10%. The second one is designed for an ultra-broadband of 4.6–14 μm, which is actually implemented by cleverly connecting two bands of 4.6–6.1 μm and 6.1–14 μm. Furthermore, the presented structures exhibit low thermal emission at the same time due to the low absorption loss of silicon in the infrared spectrum, which can be regarded as an achievement of laser–infrared compatible camouflage. We believe the proposed strategy may open a new route to implement multispectral electromagnetic modulation and multiphysical engineering applications. © 2019 Chinese Laser Press

https://doi.org/10.1364/PRJ.7.000586

1. INTRODUCTION

In recent years, artificial metasurfaces have enabled rapid development of ultrathin optical devices that can modify the light wavefront by altering its phase and amplitude [1–6]. A variety of functional devices based on metasurfaces have been proposed and demonstrated, including vortex beam generators [7,8], polarization modulators[9–11], flat lenses [12–14], perfect absorbers [15], and optical holograms [16–18]. Since metasurfaces open a new route to redirect reflected wave around the object, numerous structures have been put forward and experimentally characterized to reduce the reflection and scattering of objects, resulting in desired camouflage or invisibility [19–24]. Utilizing the phase discontinuity of metasurface, the electromagnetic shape of the objects can be arbitrarily manipulated with no influence on their geometric properties. However, most current phase-gradient metasurfaces are designed in only a single spectrum with narrow bandwith. Though some dual-band and wideband approaches are achieved by vertical stacking of metasurfaces [21,25], the volume and fabrication difficulty are inevitably increased. In addition, these low-reflection metasurfaces generally cannot achieve thermal invisibility at the same time due to their high infrared absorption/emission arising from

the complex metal–dielectric composites. Recently, by combining the low thermal emission nature of metal and geometric phase, all-metallic metasurfaces have been proposed to reduce both the specular reflectance and infrared emissivity [26]. Nevertheless, the operating bandwidth is significantly limited.

In this paper, we present two metasurfaces to simultaneously implement low infrared specular reflection and emission in dual-band and ultra-broadband ranges, respectively. Both metasurfaces comprise a monolayer of amorphous silicon (α-Si) gratings with the same geometry but diverse spatial orientations deposited on a metal mirror, which can be utilized to generate dual-band and wideband high-efficiency photonic spin-orbit interaction (PSOI) and geometric phase. Theoretically, low thermal emission results from silicon, which is nearly free of loss in the infrared spectrum, and low specular reflection can be achieved by tailoring the wavefront and redirecting the reflected energy to other angles.

2. DESIGN AND METHODS

The reflected wavefront can be modified by modulating the phase of scattered wave upon structured surfaces. According to the generalized Snell's law [27,28], by properly designing
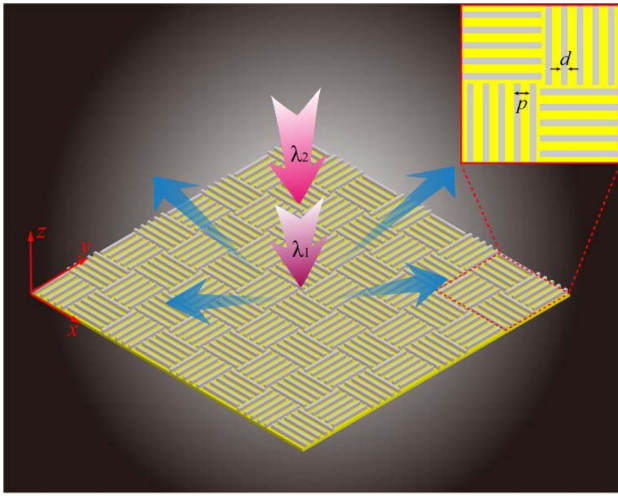
Fig. 1. Schematic of the scattering engineered metasurface with a chessboard-like configuration; λ_1 and λ_2 denote the incoming wavelengths from two infrared bands. Inset illustrates the super cell of the metasurface.

the phase distribution, the reflected light will be forced to propagate in well-defined ways with respect to the specular reflection direction. Therefore, the specular reflectance can be reduced by taking advantage of the anomalous reflection property. In the following, we focus on the geometric or so-called Pancharatnam–Berry (PB) phase [29,30]. According to the PSOI in inhomogeneous structures, under circularly polarized incidence, the cross-polarized light will be imprinted with a geometric phase that is twice the fast axes orientation angle of the half-wave plate [$\zeta(x,y)$] and can be written as $\Phi(x,y) = 2\sigma\zeta(x,y)$ [14,24]. Here, $\sigma = \pm 1$ denotes the left- and right-handed circular polarizations (LCP and RCP). In our design, the reflective half-wave plate is composed of a layer of α-Si ridges tiled on a gold (Au) mirror. Therefore, by controlling the local orientation of the fast axes of α-Si ridges between 0 and π, phase pickups can be achieved that cover the full 0-to-2π range. This provides full control over the wavefront. In the simplest case, hereafter we choose two α-Si ridge arrays with the orientation angle difference of $\Delta\zeta = \pi/2$ in a chessboard-like configuration (Fig. 1); thus, the reflection phase difference of $\Delta\Phi = \pi$ is induced between the adjacent superunits. In this alternating circumstance, the metasurface is virtually shaped just like a chessboard pattern with different step heights [31]. When an electromagnetic wave is illuminated on this structure, the light is scattered mainly in offset directions; as a consequence, the reflected energy along the specular direction is considerably reduced. Owing to its four-fold geometrical symmetry, the metasurface is insensitive to polarization states of the incident waves and can be treated as polarization independent [26]. We should note that, although here the metasurface consists of dielectric gratings with only two orthogonal orientation angles, the design can be easily extended to create more complex electromagnetic functions [14,24,26].

A. Dual-Band and Ultra-Broadband Unit Cell Design
The unit cell of our metasurface, which serves as a reflective half-wave plate, composed of a periodic birefringent α-Si ridge array placed on an Au mirror, is illustrated in Fig. 2(a), where p

is the period, w is the width of α-Si ridges, and h is the thickness of the ridges. Each ridge behaves as an anisotropic truncated waveguide and supports substantial phase retardation between the orthogonal polarizations along two main axes [14]. In practice, the thickness of the unit cells could be much smaller compared with the free-space wavelength due to the high refractive index of the semiconductors [32], especially for this reflective configuration. In the following, we first design a half-wave plate in a dual-band involving the wavelengths of 1.06 μm and 10.6 μm, which are two significant wavelengths for lasers in near- and far-infrared regimes. The geometric parameters are $p = 0.58$ μm, $w = 0.3$ μm, and $h = 1.3$ μm. The reflection amplitude and phase for the unit cells under x- (TM) and y- (TE) polarized waves are calculated using CST Microwave Studio with periodic boundary condition. Figure 2(b) shows the calculated phases for the orthogonal polarizations from 20 THz to 300 THz as well as the relative phase difference ($\Delta\Phi = \Phi_y - \Phi_x$). Attributed to the dispersion difference between two orthogonal directions and strong resonances supported by the α-Si array, one can see that [shadow area in Fig. 2(b)] the phase shift at around 277–286 THz (1.05–1.08 μm) and 25–60 THz (5–12 μm) is close to π and $-\pi$, respectively. The corresponding reflectances for cross-polarized and co-polarized components under circularly polarized illumination are calculated as depicted in Fig. 2(c). We observe that the co-polarized reflectance at 1.05–1.08 μm and 5–12 μm is less than 10%; correspondingly, the cross-polarized reflectance is higher than 90%, indicating that the α-Si ridges can serve as a dual-band reflective half-wave plate. The reflected electric field distributions under TE and TM incidence at the wavelengths of 1.06 μm and 10.6 μm are given in Figs. 2(d) and 2(f), respectively; π phase retardation between the two orthogonal directions can be observed. We also provide the reflected phase profiles at 1.06 μm and 10.6 μm to further verify the desired phase delay, as shown in Figs. 2(e) and 2(g). In addition, we note that the electric fields in the gap between two ridges for TM illumination can be fitted to a catenary shape, which is according to previously reported catenary optics [24,33,34]; the generalized catenary model and fittings are given in Appendix A. As a common semiconductor material, the silicon ridge supports complex resonances not only responsible for the dual-band polarization conversion, but also can support ultra-broadband PSOI. As shown in Fig. 2(h), a wideband and high-efficiency polarization conversion in 4.6–4 μm is obtained by connecting two bands of 4.6–6.1 μm and 6.1–14 μm. The corresponding geometric parameters of the α-Si ridge are $p = 3.8$ μm, $w = 1.1$ μm, and $h = 1.9$ μm. To get a clearer visualization of this broadband effect, we provide the spectra of reflection amplitude and phase under TE and TM illuminations, as depicted in Figs. 2(i) and 2(j). A sharp reflection dip at 49.4 THz (6.1 μm) and 2π jump of phase shift from 49 THz to 50 THz can be found for the TM wave, leading to an abrupt phase retardation between the two orthogonal polarizations, as illustrated in Fig. 2(k). The substantial swing in phase shift for TM wave is attributed to the mode transformation, which can be seen from the magnetic field distributions in Fig. 2(m); the α-Si ridges support a first-order resonance at 49 THz but a second-order resonance

Dual-band unit cell   **Ultra-broadband unit cell**
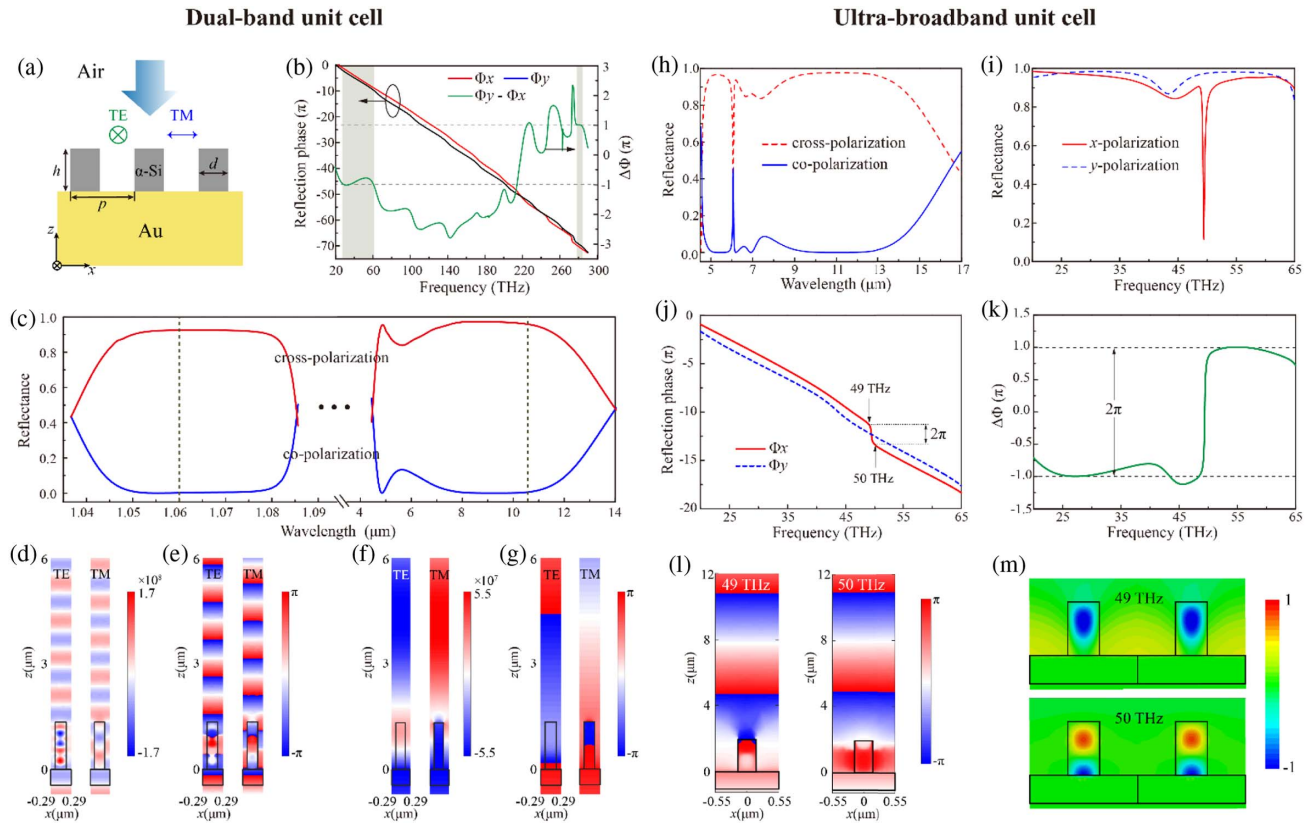
Fig. 2. Numerically calculated results of the (a)–(g) dual-band and (h)–(m) ultra-broadband unit cells. (a) Schematic view of a periodic α-Si ridge array on a gold mirror. (b) Reflection phase for the unit cells under x- (TM) and y- (TE) polarized incidences, as well as the relative phase difference between x and y polarizations. (c) Cross-polarization and co-polarization reflectances under circularly polarized illumination at near-infrared and far-infrared spectra. (d), (e) Calculated (d) electric field distributions and (e) phase profiles for TE- and TM-polarized illuminations at 1.06 μm. (f), (g) Calculated (f) electric field distributions and (g) phase profiles for TE- and TM-polarized illuminations at 10.6 μm. (h) Ultra-broadband cross-polarization and co-polarization reflectances under circularly polarized illumination. (i), (j) Calculated (i) reflectance and (j) phase for TE and TM illuminations. (k) Phase difference between the two orthogonal polarizations. (l) Phase distributions for TM illumination at 49 THz and 50 THz. (m) Magnetic field profiles for TM illumination at 49 THz and 50 THz.

at 50 THz. The above results confirm that our designs can supply dual-band and ultra-broadband reflective half-wave plates.

B. Full-Model Calculation and Simulation

In the following, we focus on the full-model calculation and simulation. As shown in Fig. 3, when electromagnetic waves illuminate on the chessboard-like metasurface, the directions of the reflection field can be predicted based on a theoretical basic. Assuming the incident wavelength is λ and the incident angle is (θ_0, φ_0), the dimensions of the super-units for the metasurface are d_x and d_y, respectively. The reflection field direction (θ, φ) can be calculated by [35]

$$\tan \varphi = \frac{\sin \theta_0 \sin \varphi_0 \pm (2n+1)\frac{\lambda}{2d_y}}{\sin \theta_0 \cos \varphi_0 \pm (2m+1)\frac{\lambda}{2d_x}}, \tag{1}$$

$$\sin \theta = \frac{\sin \theta_0 \sin \varphi_0 \pm (2n+1)\frac{\lambda}{2d_y}}{\sin \varphi}$$
$$= \frac{\sin \theta_0 \cos \varphi_0 \pm (2m+1)\frac{\lambda}{2d_x}}{\cos \varphi}, \tag{2}$$

where θ and φ are the elevation and azimuth angles, respectively. $n + m + 1$ defines the order of the grating lobes regarding the chessboard structure. Assuming $d_x = d_y$, under normal incidence ($\theta_0 = \varphi_0 = 0°$), the first-order grating lobes ($n = m = 0$) are expected as

$$\tan \varphi = \pm \frac{d_x}{d_y} = \pm 1, \tag{3}$$

$$\sin \theta = \pm \frac{\lambda}{\sqrt{2}d_y} = \pm \frac{\lambda}{\sqrt{2}d_x}. \tag{4}$$

This is to say that the backscattered energy is redirected mainly to four diagonal directions in the 45° planes ($\varphi = 45°$ and 135°). For the dual-band metasurface, each super-unit comprises 20 periodic α-Si ridges (i.e., $d_x = d_y = 11.6$ μm). According to Eq. (4), $\theta = \pm 3.7°$ and $\theta = \pm 40°$ can be obtained at $\lambda = 1.06$ μm and $\lambda = 10.6$ μm, respectively. For the ultra-wideband metasurface, each super-unit is set to consist of five periodic α-Si ridges (i.e., $d_x = d_y = 19$ μm), and the elevation angle θ increases from 9.8° to 31.4° with respect to the incident wavelength changing from 4.6 μm to 14 μm.

**Dual-band metasurface**   **Ultra-broadband metasurface**
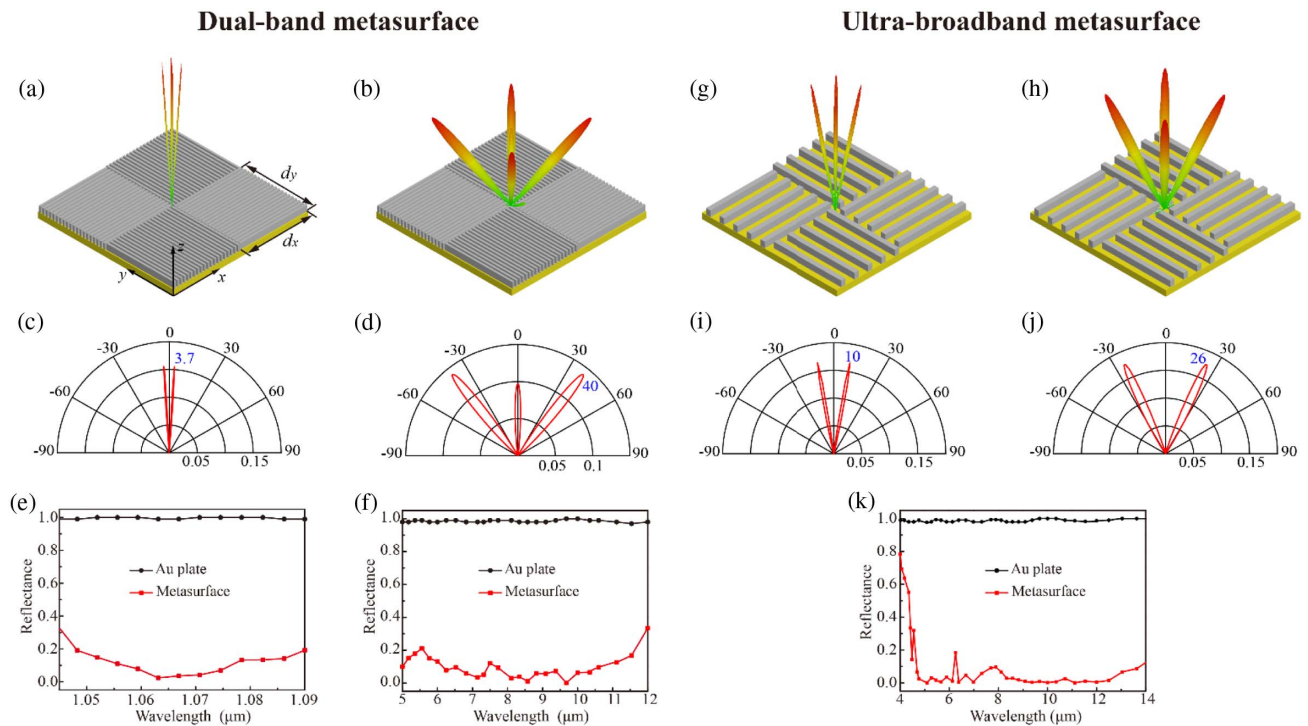
Fig. 3. Full-wave simulations for the (a)–(f) dual-band and (g)–(k) ultra-broadband metasurfaces for *x*-polarized normal incidences. (a), (b) 3D scattering patterns of the dual-band metasurface at 1.06 µm and 10.6 µm, respectively. (c), (d) Scattering patterns of the dual-band metasurface on $\varphi = 45°$ plane at 1.06 µm and 10.6 µm, respectively. (e), (f) Calculated specular reflectance spectra of the dual-band metasurface and an Au plate. (g), (h) 3D scattering patterns of the ultra-broadband metasurface at 5 µm and 12 µm, respectively. (i), (j) Scattering patterns of the ultra-broadband metasurface on $\varphi = 45°$ plane at 5 µm and 12 µm, respectively. (k) Calculated specular reflectance spectra of the ultra-broadband metasurface and an Au plate.

It should be noted that although the specular reflection can be completely suppressed theoretically, it is actually limited by the polarization conversion efficiency of the metasurface according to the PSOI. Thus, full-wave simulations are performed to check the performance of these devices. A subgroup made of 2 × 2 super-units with mutually orthogonal orientations is simulated with periodic boundaries. For the dual-band metasurface, the simulated three-dimensional (3D) scattering patterns for *x*-polarized normal incidence at 1.06 µm and 10.6 µm are illustrated in Figs. 3(a) and 3(b). As described theoretically by this model, it presents a minimum value at $\theta = 0°$ (*z* direction), and the power is scattered in the 45° planes ($\varphi = 45°$ and 135°). We also provide the corresponding $\varphi = 45°$ (or 135°) plane scattering pattern of the metasurface in Figs. 3(c) and 3(d). The scattering elevation angle θ is in good agreement with the theoretic predictions. In Fig. 3(d), we can see that the reflectance at $\theta = 0°$ is not zero. This is due to the fact that the structure is not a perfect half-wave plate at $\lambda = 10.6$ µm. However, the reflectance is still reduced to be less than 0.1. The simulated near-infrared and far-infrared reflectance spectra of the metasurface are also given in Figs. 3(e) and 3(f). Similarly, the simulated results for the ultra-broadband metasurface are illustrated in Figs. 3(g)–3(k). Figures 3(g)–3(j) show the 3D and $\varphi = 45°$ plane scattering patterns at the wavelengths of 5 µm and 12 µm, and Fig. 3(k) illustrates the simulated specular reflectance spectrum of the metasurface; excellent broadband reflection reduction can be observed.

3. EXPERIMENT AND DISCUSSION

In experiment, to reduce the fabrication difficulty and make it easy for experimental characterization, the ultra-broadband metasurface sample is considered and fabricated with an area of 14 mm × 14 mm by using conventional photolithography techniques. The fabrication procedure is presented in Fig. 4(a). First, an Au layer as the mirror with a thickness of 200 nm is sputtered on a 2 mm thick quartz substrate using magnetron sputtering. Then a layer of α-Si with the thickness of 1.9 µm is deposited upon the Au film, and a 500 nm thick AZ1500 photoresist layer is coated on the α-Si film. The target pattern is formed by laser direct writing on the upper photoresist. Subsequently, the pattern is transferred into the α-Si film using reactive ion etching (RIE). Finally, the residual photoresist is removed by dipping it into acetone, and the sample is formed. The scanning electron microscope (SEM) image of part of the fabricated metasurface is shown in Fig. 4(b) [center of Fig. 4(a)].

The reflectance of the sample is measured using the Fourier transform infrared (FTIR) spectrometer. A pair of off-axis concave mirrors is used to collect and collimate the beams, and they are both mounted on guide rails and fixed with an infrared emitter and detector, respectively. The incident and reflected angles can be easily changed by rotating the guide rails. However, due to the geometric dimension limit of the concave mirrors, the specular angle can be adjusted only by larger than 15°. Therefore, we choose three specular angles, –15°, 20°, and 30°,
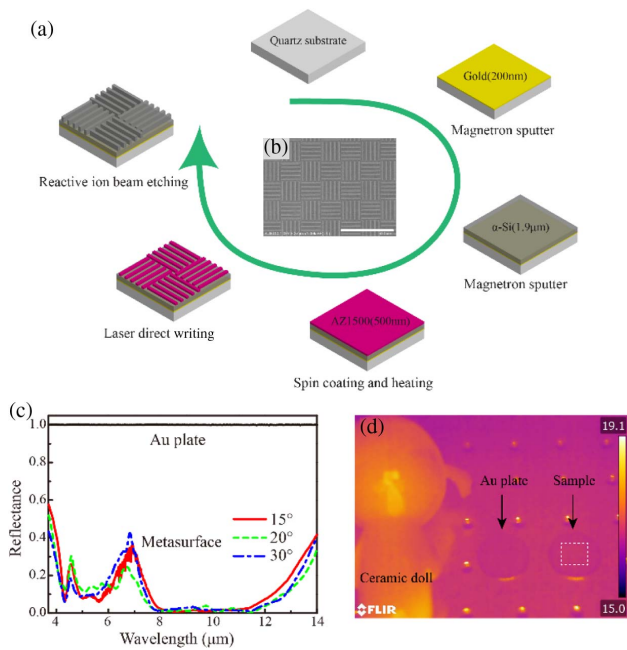
Fig. 4. Sample fabrication and measurements. (a) Schematic of the fabrication process. (b) SEM image of part of the fabricated metasurface. Scale bar: 50 μm. (c) Measured reflectance spectra of the fabricated sample and Au plate under oblique incidences. (d) Measured thermal infrared images of a ceramic doll, a gold plate, and the fabricated sample. The white dotted frame marks the fabricated area.

for measurements. The measured reflectances under polarization-independent incidence in 4–14 μm are recorded in Fig. 4(c). For comparison, a same-sized Au plate without the subwavelength gratings is also measured. We observe that the specular reflectance of the metasurface is less than 0.1 μm from 4.6 μm to 6 μm and 7.5 μm to 13 μm for all the incidence angles. The overall results of the measured reflection spectra qualitatively agree with the predicted spectra, while the slight difference between the measurements and simulations may be attributed to the fabrication imperfections and polarization-independent oblique incidences (see Appendix B). In general, the obtained results indicate that our structure has excellent performance in suppressing the specular reflection over broadband and wide incidence angles.
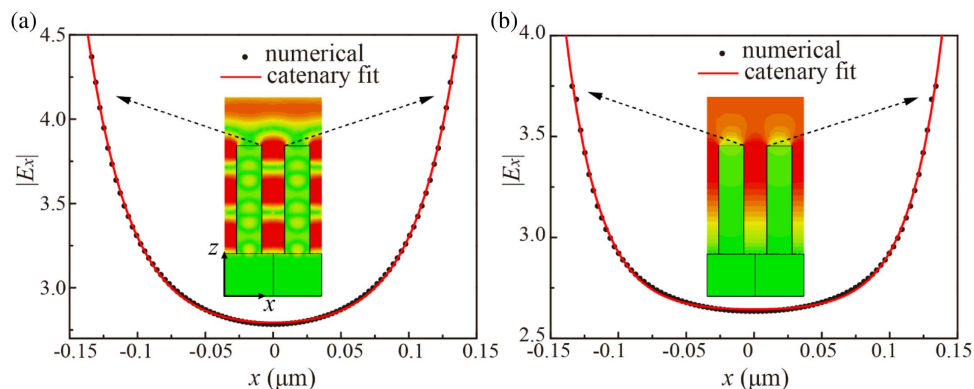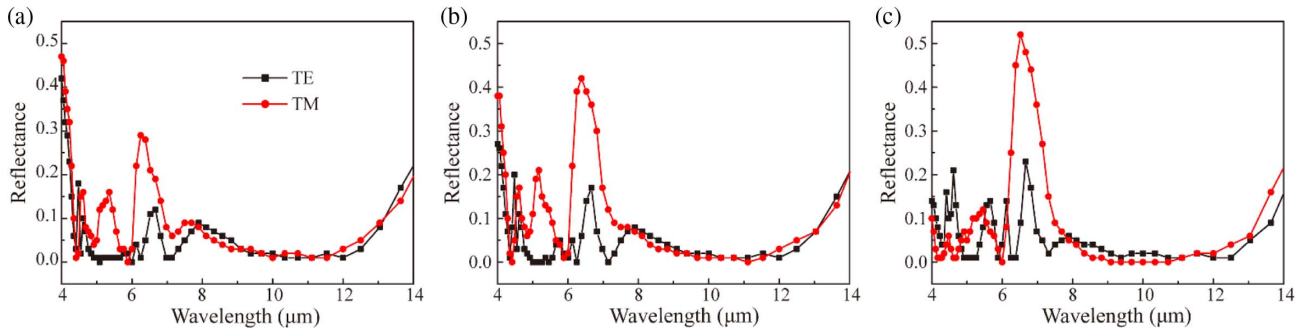
In addition, since silicon is nearly free of loss in mid- and far-infrared spectra and our designed metasurface is composed of just a layer of α-Si ridges on top of an Au mirror, the structure still exhibits low thermal infrared emission. Here, we compare the surface emissivity of the metasurface sample and a gold plate measured by a commercial thermal infrared imager to illustrate this issue. The measurement is performed at room temperature (20°C), and the results are shown in Fig. 4(d). The fabricated sample, a ceramic doll, and a bare gold plate are placed on a metallic optical platform. By comparing their measured temperatures, we find that the surface emission of the metasurface and the metallic plate is much lower than that of the ceramic doll, and the metasurface exhibits low emissivity comparable to that of a flat gold plate (<0.1; the theoretic calculations and comparison can be seen in Appendix C).

4. CONCLUSION

In summary, we have presented a kind of single-layer silicon-based metasurface to achieve high-efficiency dual-band and ultra-broadband geometric phase modulation in infrared regime. Simultaneous low specular reflection and low thermal emission behaviors have been performed by combining low-infrared-loss materials and high-efficiency PSOI in subwavelength structures. The simulated and measured results show excellent specular reflection reduction in dual-band, broad spectrum, and wide incident angles. To our knowledge, this is the first time to achieve wavefront manipulation for simultaneous 1.06 μm and 10.6 μm, as well as broad operating bandwidth ratio over 3:1 by using only a single-layer dielectric metasurface. Also, this design method as well as the fabrication process is universal and can be easily applied in other spectra. We believe these multifunctional metasurfaces are promising candidates to achieve multispectral and multiphysical applications such as laser-infrared compatible stealth. In addition, this approach can be applied to design tunable metasurfaces, which has more extensive applications [36].

APPENDIX A: CATENARY OPTICAL FIELDS

Figures 5(a) and 5(b) show the calculated electric field magnitude distributions E_x of the α-Si array under x-polarized incidence at the wavelengths of 1.06 μm and 10.6 μm, respectively.

Fig. 5. Simulated electric field magnitude distributions E_x in the gap between two α-Si ridges under x-polarized illumination and the catenary curves fitting at the wavelength of (a) 1.06 μm and (b) 10.6 μm, respectively.

Fig. 6. Full-wave simulated specular reflectance spectra of the metasurface under oblique incidences of (a) 15°, (b) 20°, and (c) 30°, respectively.

One can see that there are strong localized field enhancements in the gap between two α-Si ridges for E_x component. The electric fields in the gap between two ridges can be fitted to a catenary shape. The magnitudes of the E_x along the center of the gap are given together with the curves fitted by generalized catenary function:

$$|E_x| = a \exp(bx) + c \exp(dx) + e, \qquad (A1)$$

where a, b, c, d, and e are the variables in the generalized catenary function. For the wavelength of 1.06 μm, the fitting coefficients, respectively, are $a = c = 0.024$, $b = d = 31.53$, and $e = 2.746$ with R-square equal to 0.9996. For the wavelength of 10.6 μm, the fitting coefficients, respectively, are $a = c = 0.054$, $b = d = 39.90$, and $e = 2.63$ with R-square equal to 0.9985. We observe that both catenary curves (solid curves) can well approach the simulated electric field profiles (dotted curves).

APPENDIX B: FULL-WAVE SIMULATIONS UNDER OBLIQUE INCIDENCES

Although the chessboard-like configuration has four-fold geometrical symmetry and thus is insensitive to the polarization
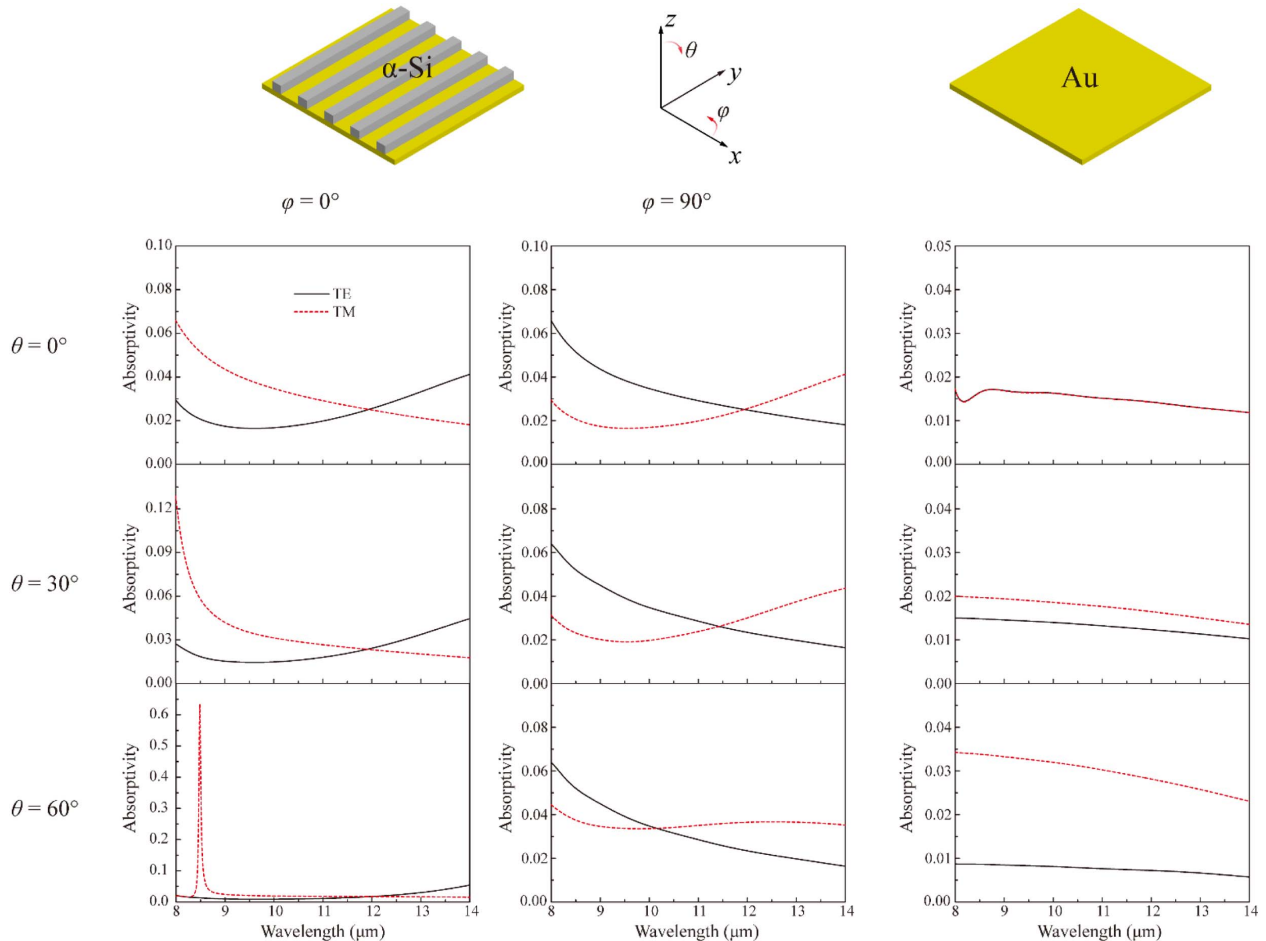
Fig. 7. Calculated absorption spectra of a gold plate with and without the α-Si ridge array under TE and TM illuminations with different incidence angles.

states of normally incident waves, under oblique illuminations, there will be some differences between TE and TM polarizations. Figure 6 shows the full-wave simulated specular reflectances of the broadband metasurface under the incidences of 15°, 20°, and 30°. The resonances at the short wavelengths are attributed to high-order diffraction under oblique incidences. Considering that the incident light is polarization independent in the experiment, the measured results [Fig. 4(c) of the main text] are in good agreement with the simulations.

APPENDIX C: NUMERICAL CALCULATIONS OF EMISSIVITY

Here, we calculate the emissivity of an α-Si ridge array deposited on a gold plate. According to Kirchhoff's thermal radiation law, emissivity (E) equals absorptivity (A) when the material is in the condition of thermal equilibrium, i.e., $E = A$. Thus the surface emissivity of the α-Si array can be obtained by calculating its infrared absorptivity, as shown in Fig. 7, first and second columns. For comparison, the emissivity/absorptivity of a bare gold plate has also been calculated, as illustrated in Fig. 7, third column. One can see that the absorption of the structure with α-Si ridges is a little higher than that of the bare gold mirror. However, the mean values are still below 0.1. The absorption peak at 8.5 μm for 60° TM illumination originates from the ohmic loss of surface electromagnetic wave propagating along the metallic surface under oblique incidence.

REFERENCES

1. N. Yu and F. Capasso, "Flat optics with designer metasurfaces," Nat. Mater. **13**, 139–150 (2014).
2. N. Meinzer, W. L. Barnes, and I. R. Hooper, "Plasmonic meta-atoms and metasurfaces," Nat. Photonics **8**, 889–898 (2014).
3. X. Luo, D. Tsai, M. Gu, and M. Hong, "Extraordinary optical fields in nanostructures: from sub-diffraction-limited optics to sensing and energy conversion," Chem. Soc. Rev. (2019), DOI: 10.1039/c8cs00864g.
4. X. Luo, "Engineering optics 2.0: a revolution in optical materials, devices, and systems," ACS Photon. **5**, 4724–4738 (2018).
5. X. Luo, D. Tsai, M. Gu, and M. Hong, "Subwavelength interference of light on structured surfaces," Adv. Opt. Photon. **10**, 757–842 (2018).
6. X. Luo, "Subwavelength artificial structures: opening a new era for engineering optics," Adv. Mater. **31**, 1804680 (2018).
7. M. Pu, X. Li, X. Ma, Y. Wang, Z. Zhao, C. Wang, C. Hu, P. Gao, C. Huang, and H. Ren, "Catenary optics for achromatic generation of perfect optical angular momentum," Sci. Adv. **1**, e1500396 (2015).
8. J. Zeng, L. Li, X. Yang, and J. Gao, "Generating and separating twisted light by gradient-rotation split-ring antenna metasurfaces," Nano Lett. **16**, 3101–3108 (2016).
9. N. K. Grady, J. E. Heyes, D. R. Chowdhury, Y. Zeng, M. T. Reiten, A. K. Azad, A. J. Taylor, D. A. Dalvit, and H.-T. Chen, "Terahertz metamaterials for linear polarization conversion and anomalous refraction," Science **340**, 1304–1307 (2013).
10. M. Pu, P. Chen, Y. Wang, Z. Zhao, C. Huang, C. Wang, X. Ma, and X. Luo, "Anisotropic meta-mirror for achromatic electromagnetic polarization manipulation," Appl. Phys. Lett. **102**, 131906 (2013).
11. X. Ma, M. Pu, X. Li, Y. Guo, and X. Luo, "All-metallic wide-angle metasurfaces for multifunctional polarization manipulation," Opto-Electron. Adv. **2**, 180023 (2019).
12. M. Khorasaninejad, W. T. Chen, R. C. Devlin, J. Oh, A. Y. Zhu, and F. Capasso, "Metalenses at visible wavelengths: diffraction-limited focusing and subwavelength resolution imaging," Science **352**, 1190–1194 (2016).
13. S. Wang, P. C. Wu, V.-C. Su, Y.-C. Lai, C. H. Chu, J.-W. Chen, S.-H. Lu, J. Chen, B. Xu, and C.-H. Kuan, "Broadband achromatic optical metasurface devices," Nat. Commun. **8**, 187 (2017).
14. D. Lin, P. Fan, E. Hasman, and M. L. Brongersma, "Dielectric gradient metasurface optical elements," Science **345**, 298–302 (2014).
15. Y. Wang, X. Ma, X. Li, M. Pu, and X. Luo, "Perfect electromagnetic and sound absorption via subwavelength holes array," Opto-Electron. Adv. **1**, 180013 (2018).
16. X. Ni, A. V. Kildishev, and V. M. Shalaev, "Metasurface holograms for visible light," Nat. Commun. **4**, 2807 (2013).
17. G. Zheng, H. Mühlenbernd, M. Kenney, G. Li, T. Zentgraf, and S. Zhang, "Metasurface holograms reaching 80% efficiency," Nat. Nanotechnol. **10**, 308–312 (2015).
18. X. Li, L. Chen, Y. Li, X. Zhang, M. Pu, Z. Zhao, X. Ma, Y. Wang, M. Hong, and X. Luo, "Multicolor 3D meta-holography by broadband plasmonic modulation," Sci. Adv. **2**, e1601102 (2016).
19. D. S. Dong, J. Yang, Q. Cheng, J. Zhao, L. H. Gao, S. J. Ma, S. Liu, H. B. Chen, Q. He, and W. W. Liu, "Terahertz broadband low-reflection metasurface by controlling phase distributions," Adv. Opt. Mater. **3**, 1405–1410 (2015).
20. T. J. Cui, M. Q. Qi, X. Wan, J. Zhao, and Q. Cheng, "Coding metamaterials, digital metamaterials and programmable metamaterials," Light: Sci. Appl. **3**, e218 (2014).
21. M. Pu, Z. Zhao, Y. Wang, X. Li, X. Ma, C. Hu, C. Wang, C. Huang, and X. Luo, "Spatially and spectrally engineered spin-orbit interaction for achromatic virtual shaping," Sci. Rep. **5**, 9822 (2015).
22. X. Ni, Z. J. Wong, M. Mrejen, Y. Wang, and X. Zhang, "An ultrathin invisibility skin cloak for visible light," Science **349**, 1310–1314 (2015).
23. Y. Yang, L. Jing, B. Zheng, R. Hao, W. Yin, E. Li, C. M. Soukoulis, and H. Chen, "Full-polarization 3D metasurface cloak with preserved amplitude and phase," Adv. Mater. **28**, 6866–6871 (2016).
24. X. Xie, M. Pu, Y. Huang, X. Ma, X. Li, Y. Guo, and X. Luo, "Heat resisting metallic meta-skin for simultaneous microwave broadband scattering and infrared invisibility based on catenary optical field," Adv. Mater. Technol. **4**, 1800612 (2018).
25. J. Yang, C. Huang, X. Wu, B. Sun, and X. Luo, "Dual-wavelength carpet cloak using ultrathin metasurface," Adv. Opt. Mater. **6**, 1800073 (2018).
26. X. Xie, X. Li, M. Pu, X. Ma, K. Liu, Y. Guo, and X. Luo, "Plasmonic metasurfaces for simultaneous thermal infrared invisibility and holographic illusion," Adv. Funct. Mater. **28**, 1706673 (2018).
27. N. Yu, P. Genevet, M. A. Kats, F. Aieta, J.-P. Tetienne, F. Capasso, and Z. Gaburro, "Light propagation with phase discontinuities: generalized laws of reflection and refraction," Science **334**, 333–337 (2011).
28. X. Luo, "Principles of electromagnetic waves in metasurfaces," Sci. China Phys. Mechan. Astron. **58**, 594201 (2015).
29. S. Pancharatnam, "Generalized theory of interference and its applications," Proc. Indian Acad. Sci. A **44**, 247–262 (1956).
30. M. V. Berry, "The adiabatic phase and Pancharatnam's phase for polarized light," J. Mod. Opt. **34**, 1401–1407 (1987).
31. S. Simms and V. Fusco, "Chessboard reflector for RCS reduction," Electron. Lett. **44**, 316–318 (2008).
32. E. D. Palik, *Handbook of Optical Constants of Solids* (Academic, 1985).
33. M. Pu, Y. Guo, X. Li, X. Ma, and X. Luo, "Revisitation of extraordinary Young's interference: from catenary optical fields to spin-orbit interaction in metasurfaces," ACS Photon. **5**, 3198–3204 (2018).

34. M. Pu, X. Ma, Y. Guo, X. Li, and X. Luo, "Theory of microscopic metasurface waves based on catenary optical fields and dispersion," Opt. Express **26**, 19555–19562 (2018).

35. J. C. I. Galarregui, A. T. Pereda, J. L. M. De Falcon, I. Ederra, R. Gonzalo, and P. de Maagt, "Broadband radar cross-section reduction using AMC technology," IEEE Trans. Antennas Propag. **61**, 6136–6143 (2013).

36. A. Nemati, Q. Wang, M. Hong, and J. Teng, "Tunable and reconfigurable metasurfaces and metadevices," Opto-Electron. Adv. **1**, 180009 (2018).